

Feed-Forward Compensation of Body-Pointing Uncertainties for Laser Communication Terminals

René Rüdtenklau^{*†}, Salvatore Barone[‡], Elisa Garbagnati[§], and Simon Spier[¶]
German Aerospace Center (DLR), Institute of Communications and Navigation, Weßling, Germany, 82234

Georg Schitter^{||}
Technical University Wien, Mechatronics and Power Electronics Institute, Vienna, Austria, 1040

Nomenclature

| | | |
|----------------------|---|--|
| A | = | gain error matrix, a.u. |
| C | = | calibrated gain error matrix, a.u. |
| ω | = | true rate vector, deg s ⁻¹ |
| $\tilde{\omega}$ | = | measured rate vector, deg s ⁻¹ |
| $\hat{\omega}$ | = | calibrated rate vector, deg s ⁻¹ |
| o | = | offset rate vector, deg s ⁻¹ |
| b | = | calibrated offset rate vector, deg s ⁻¹ |
| v | = | sensor noise vector, deg s ⁻¹ |
| $I_{3 \times 3}$ | = | identity matrix, a.u. |
| q | = | quaternion, a.u. |
| $\Xi(q)$ | = | quaternion matrix, a.u. |
| q_{err} | = | pointing error quaternion, a.u. |
| $[q_{1:3}]_{\times}$ | = | quaternion's cross product, a.u. |
| \hat{q} | = | estimated quaternion, a.u. |
| Λ | = | attitude (DCM) matrix, a.u. |
| $\hat{\Lambda}$ | = | estimated attitude (DCM) matrix, a.u. |
| $\tilde{\Lambda}$ | = | attitude (DCM) error matrix, a.u. |
| ψ | = | combined LCT and ADCS (Euler) angles, deg |
| θ | = | optical terminal (Euler) angles, deg |
| μ_{θ} | = | mean of optical terminal (Euler) angles, deg |

*Research associate, Optical Satellite Links, rene.rueddenklau@dlr.de

†PhD candidate, Mechatronics and Power Electronics Institute

‡Student, Optical Satellite Links

§Research associate, Optical Satellite Links

¶Student, Optical Satellite Links

||Professor, Mechatronics and Power Electronics Institute

| | | |
|----------------------------|---|---|
| σ_θ | = | standard deviation of optical terminal (Euler) angles,deg |
| σ_{FOU} | = | field of uncertainty standard deviation, deg |
| $\boldsymbol{\varepsilon}$ | = | attitude error vector, deg |
| α | = | pointing error angle, deg |
| \boldsymbol{r} | = | inertial reference direction, a.u. |
| \boldsymbol{u} | = | direction in body frame, a.u. |
| $\hat{\boldsymbol{u}}$ | = | estimated direction in body frame, a.u. |
| $\boldsymbol{\phi}$ | = | true ADCS pointing angles, deg |
| $\hat{\boldsymbol{\phi}}$ | = | gyroscope propagated angles, deg |
| G | = | amplitude, rad s^{-1} |
| f | = | frequency, rad s^{-1} |
| d | = | phase, rad |
| M | = | magnification, a.u. |
| t | = | time, s |
| \boldsymbol{R} | = | rotation matrix , a.u. |

I. Introduction

Free-space optical communication is achieved by low-divergent laser beams, which require precise pointing. Precise host platform pointing is required, especially for a CubeSat-sized laser communication terminal (LCT), which often waives the use of a dedicated hemispherical pointing assembly. Moreover, a high degree of pointing stability is necessary to facilitate the successful acquisition process for inter-satellite links. In general, the supplier of the satellite bus and the laser communication terminal are two distinct entities [1]. Consequently, valuable information regarding the attitude is often not shared at a sufficient update rate between the involved systems.

Known efforts to make use of exchanging data about attitude knowledge are presented in recent works [2, 3]. A common scenario is based on the relative attitude information of the optical payload with respect to a beacon as an additional input for the spacecraft's Kalman attitude estimation filter. This enables sub-arcsecond pointing accuracy and increased stability during an optical link [4]. It is especially useful when the satellite experiences highly dynamic scenarios such as zenith overflights during a direct to earth (DTE) link, pointing towards an optical ground station (OGS), or in an inter-satellite link (ISL) when the relative orientation to the other satellite has to be maintained with very high accuracy. In contrast, the approach proposed in this work targets primarily scenarios where the link is not yet established, the so called acquisition phase.

For this phase, a common approach to compensate for instabilities is the use of secondary sensors such as gyroscopes

within the attitude control system [1]. A general usage of gyroscope sensors for stabilization is known from camera stabilizing gimbals or free-space optical gimbals. One method uses the measured drift rates to compensate disturbances within the velocity path of a closed-loop controller in combination with an observer model [5]. However, inter-subsystem knowledge of the attitude is not used. Primarily, information within the gimbal subsystem is exploited to reach the pointing goal, only relying on one type of sensor. Another aspect of this approach is that highly accurate gyroscope sensors have to be used in order to have a standalone stabilizing support for the main attitude controller.

Although such precise gyroscopes are available, for example fiber optic gyroscopes which promise high sensitivities, they do not fit the size, weight and power constraints of a CubeSat sized LCT [6]. But there are ongoing efforts of development approaches that target the use case of micro satellites to implement so called integrated optical gyroscopes with commercial of the shelf components in a small form factor [7] or even as photonic integrated circuits [8]. In this work, however, only commercially available solutions are considered which need to fit on a printed circuit board (PCB) in the CubeSat PC/104 standard together with the rest of the optical payload. The PCB itself will be mounted to the optomechanics, ensuring a fixed orientation between optics and sensors. Further, it is proposed to make use of the attitude determination and control system (ADCS) system which provides highly accurate information during the acquisition phase, where no optical feedback is available. The disadvantage of its relatively slow sampling rate of usually 1 Hz is then enhanced by propagation with the onboard gyroscope sensor of the LCT.

This work's main contribution proposes a concept that combines the attitude data of the ADCS and LCT secondary rate sensors and demonstrates its feasibility for augmenting attitude knowledge during pointing without optical feedback, thus mitigating body pointing uncertainties and relative mounting inaccuracies, and consequently reduces the time required for the acquisition phase. Therefore, at first, state-of-the-art CubeSat Platforms and the expected disturbances are analyzed in Section II. With this information at hand, in Section III, the methods for deriving the calibration between involved subsystems, alongside the formulation of relevant estimation algorithms and the details of the feed-forward compensation concept are introduced. Finally, Section IV discusses the selection of the propagation algorithm by simulation and analyzes the results of the performance on a hardware-in-the-loop breadboard.

II. Inter-Satellite Link Scenario on 6U CubeSats

Optical links, especially between two LCTs, impose high accuracy requirements on the ADCS due to the narrow divergence of the laser beam. The following section evaluates state-of-the-art CubeSat platforms, in order to quantify the challenges that must be overcome to reliably establish and maintain a laser communications link. This is relevant because CubeSats represent an emerging use case for LCTs, although they have limitations concerning their ADCS with respect to larger satellites. A 6-unit CubeSat platform is used as a reference to numerically analyze the performance improvements obtained. This includes the disturbances present in the proposed scenario. Using the given infrastructure on a CubeSat, a propagation algorithm and an attitude data exchange procedure are proposed to mitigate the identified

inaccuracies.

A. Disturbance Identification

The relevant disturbances are micro-vibrations and the stability of the satellite’s pointing resulting from the limited control accuracy between two consecutive ADCS updates [9]. Further, an initial pointing offset between ADCS frame and optical axis frame, due to mounting tolerances and launch loads, may occur. Section IV.B.1 gives a solution to this calibration problem. In order to compare the improvements of the proposed algorithms for dynamic disturbances, it is necessary to understand which pointing accuracy and attitude knowledge is available on state-of-the-art CubeSat platforms[10–15]. Therefore, a small selection was made and is displayed for comparison (see Tab. 1). In addition, the CubeISL [16] mission is used as reference wherever LCT design parameters are necessary for the evaluation. The same hardware prototype is used for the following hardware-in-the-loop validation measurements.

It can be seen that the measurement or estimation of the current attitude (attitude knowledge) is generally better than the accuracy achieved by the control system (attitude accuracy), as expected. It is important to note that these parameters are also dependent on the intended use case. Star trackers, which are the most accurate means of measurement available during acquisition, are more susceptible to rotations around the sensor’s surface normal [1]. Additionally, light pollution can influence the quality of measurements.

Table 1 A brief survey of selected 6U ADCS commercial of the shelf (COTS) satellite buses

| Company/Unit | Accuracy, deg | Knowledge, deg | Stability, mdeg s⁻¹ |
|--------------------------------|----------------------|-----------------------|---------------------------------------|
| AAC Clyde Space / iADCS400[10] | < 1 | 0.008 | n/a |
| Alén Space / 6U[11] | 0.2 | 0.1 | n/a |
| Blue Canyon / XB6[12] | ±0.002 (1σ) | 0.003(3σ)[1] | 0.27 |
| Gomspace / 6UPremium[13] | 0.07 | 0.056 | n/a |
| Nano Avionics / M6PMax[14] | ±0.08 (1σ) | ±0.04 (1σ) | n/a |
| DLR / 3U CubeL[15] | < 1(3σ) | n/a | 100 (3σ) |

Based on the aforementioned evaluation—and assuming that the pointing does not get worse than on a demonstrated 3U CubeSat—it can be assumed that the drift rate, which is equivalent to the pointing stability as referred to in Table 1, within the pointing accuracy yields 0.1 deg s⁻¹ in the worst case (3U CubeL). This can be assumed since larger 6U CubeSats will have improved pointing capabilities. The worst case is therefore used in the pointing, acquisition and tracking simulations [9]. All values are understood as 3σ and therefore a satellite requirement of ±0.2 deg field of uncertainty (FOU) and a knowledge of ±0.1 deg were chosen as baseline, since most of 6U platforms are capable to reach these requirements [1]. In comparison, the divergence angle of the LCT is on the order of tens of milli-degrees, and the field of view (FOV) is usually about ten times as large [16].

In Figure 1, the perturbations, acting on the attitude of the satellite with respect to the optical axis of the LCT, are

shown in the top, on the left for a T-DAT (terminal for detection, adjustment and tracking) and on the right for its link partner T-PAT (terminal for pointing, acquisition and tracking) [9]. The middle row shows the unperturbed search pattern, a 3.2 second spiral for T-PAT and a 30.2 second grid search pattern for T-DAT for a FOU of ± 0.1 deg. The resulting superposition in the bottom row shows that the perturbations result in a distorted pattern from the start of the acquisition, marked with a yellow circle, to the point of link establishment, marked with a red circle. All results are based on an acquisition simulation for an optical ISL between CubeSats [9]. When looking at increased FOU such as the envisaged ± 0.2 deg, which is beyond the FOV of the terminal, the likelihood of successful acquisition drops drastically [9]. The proposed concept aims to propagate with enough precision to identify pointing stability errors, which are beyond the accuracy of body pointing but within the capabilities of the optical terminal's fine steering mirror (FSM).

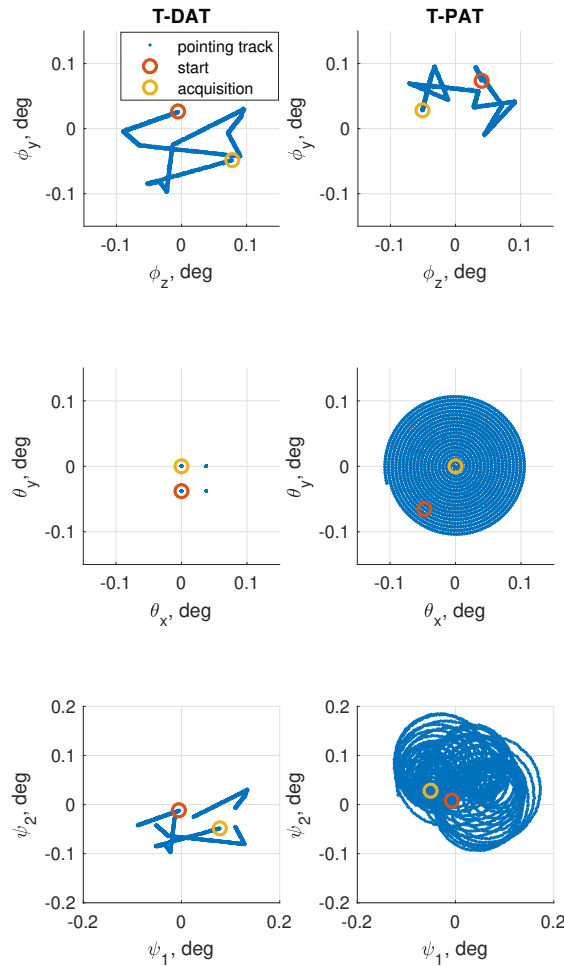


Fig. 1 Example of uncompensated search patterns being deformed due to deformation due to limited body-pointing precision.

B. Attitude Propagation and Compensation Concept

A standard CubeSat platform consists of the mechanical structure that defines the available units and the functionality provided by various subsystems. The ADCS and corresponding 6U buses can be purchased from various satellite manufacturers, allowing the user to focus on the payloads. To date, in most cases, the subsystems have been developed and operated independently. The proposed concept provides for an exchange of information between the individual subsystems in such a way that information can be shared and is commonly available even when multiple LCTs are used. A conventional ADCS operates with a high level attitude control of about 0.1 Hz to 10 Hz [17]. Thus, information from the estimation algorithm of the ADCS, which is usually a Kalman filter, can be used to reduce the FOU from the full field of regard (FOR) of the optical system to the actual FOU.

It needs to be considered that the search pattern as shown above in Figure 1 of the LCT is sampled faster—with sampling rates above those of the ADCS—on the order of several hundred to thousand times per second, since the period of a scan trajectory is directly related to the expected time needed for acquisition. Therefore, it is necessary that the update rate of the estimator matches the update rate of the optical control system. Following this train of thoughts, a separate estimation algorithm using gyroscope measurement based propagation is proposed for the control unit of the LCT, which is initialized with the estimation value of the ADCS. It is assumed that this system will generally provide more accurate information since since the ADCS utilizes the aforementioned star tracker.

However, instead of only extrapolating this initial value, the LCT makes use of its own sensor consisting of a micro-electro-mechanical system (MEMS) gyroscope sensor. This is done until the next update of the ADCS data is available. The assumption that this approach improves the attitude knowledge of the LCT is therefore investigated in this work. When comparing the two data sources, it should be noted that the sensors involved must be calibrated beforehand to align their reference frame. It should be noted that this approach is not exclusive to the use of gyroscope sensors. Alternative sensors with sufficient sampling rates, such as magnetometers, may also be employed. The methods, including the estimation and calibration algorithms, are described in more detail in Section III.

Figure 2 shows the commanding of the FSM and where the propagated information is inserted. The FSM is steered in both the acquisition phase and the tracking phase. In the latter case, the control loop is closed via the feedback from the quadrant photo diode (QPD) to the tracking controller. However, during acquisition a previously defined search pattern is executed until a beacon is detected following an acquisition scheme [9]. In order to include the measured deviation from the ideal attitude, the pointing error is added to the output of the search pattern so that the search pattern remains distortion-free with respect to the QPD's inertial frame.

III. Sensor Calibration and Attitude Augmentation

Sensors are subject to disturbances and errors, each influencing the measurements. Therefore, it is necessary to evaluate the calibration and measurement accuracy of the involved systems. Additionally, it is described how the

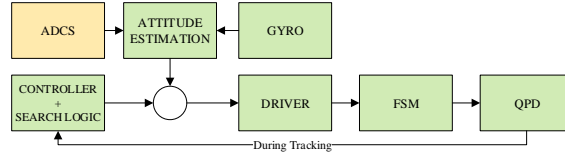


Fig. 2 Feed-forward compensation scheme using the data of the ADCS and the propagated information from the onboard gyroscope sensor.

propagation algorithm is implemented which aims to augment the a priori attitude knowledge of an LCT before the establishment of a laser link.

A. Calibration Algorithm

Each calibration error can be described as either a gain error or an additive offset. For a three dimensional vector of true values ω , the gain components make up matrices $\mathbf{A} \in \mathbb{R}^{3 \times 3}$ influencing the scaling of each axis \mathbf{A}_s , modeling cross-axis effects represented by non-orthogonality \mathbf{A}_{no} as well as mounting errors \mathbf{A}_m [18].

Equation 1 displays how the measured vector $\tilde{\omega}$ is obtained by adding the offset vector \mathbf{o} and the sensor noise ν

$$\tilde{\omega} = \underbrace{(\mathbf{A}_{no} \mathbf{A}_s \mathbf{A}_m)}_{\mathbf{A}} \cdot \omega + \mathbf{o} + \nu. \quad (1)$$

A calibration algorithm aims to determine the influence of the matrix \mathbf{A} and the offset \mathbf{o} , while the sensor noise cannot be accounted for. Therefore, the calibrated vector $\hat{\omega}$ is influenced by the measurement noise from $\tilde{\omega}$, while $\mathbf{C} = \mathbf{A}^{-1}$ and $\mathbf{b} = -\mathbf{o}$. Thus, Equation 2 shows how a measurement is transformed after the twelve calibration parameters have been determined

$$\hat{\omega} = \mathbf{C} \cdot (\tilde{\omega} + \mathbf{b}). \quad (2)$$

1. Static Calibration of the Gyroscope Sensor

The calibration of the gyroscope sensor uses the reference value of the satellite's ADCS to adjust the measurements. This is done using a standard least squares method (LSM) [19]. It is important that the measurements include motion at various velocities and on each axis to obtain acceptable results. Otherwise, over-fitting to limited sample sets may occur which can ultimately lead to erroneous results. MEMS gyroscope sensors suffer from the mentioned bias errors as well as gain errors and additionally non-orthogonality but do usually not get damaged by launch vibration loads, therefore a pre-flight calibration can be used as a reference for an on-orbit calibration [20]. The result is required for the following processing steps and is shown in Section IV.B.1.

2. Online Bias Calibration of the Gyroscope Sensor

The LSM is a batch-type static procedure, which means that a data set must be obtained by rotating the satellite beforehand. Since the quality of the calibration is highly dependent on the variety of platform motions during those measurements as well as the gyroscope's susceptibility to temperature changes that induce bias drifts, the calibration has to be verified during early operations. In order to compensate ever changing environmental conditions, a recursive bias estimation algorithm is proposed to dynamically adapt to changes affecting sensor readings.

Taking into account the proposed system architecture (see Fig. 2), the satellite ADCS will provide the terminal with its precise estimate of the attitude quaternion. Using this information, two successive attitudes can be used to estimate the true angular velocity ω of the laser terminal. This is either directly derived from the ADCS or by the derivative indicated by the Laplace variable s in Figure 3. The bias can be estimated with Equation 3 by comparing this estimated angular velocity with an average of the measurements from the onboard gyroscope sensor between two ADCS updates. As a result, the current measurement can be calibrated with the updated parameter in Equation 2

$$\mathbf{b}_{\text{gyro}} = \omega_{\text{ADCS}} - \hat{\omega}_{\text{gyro, mean}}. \quad (3)$$

However, this online calibration process has to be used with care. Scenarios with higher accelerations may lead to wrong averages of the transmitted satellite mean angular velocity. Therefore the averaging should take several samples into account but only when the velocity change between two consecutive updates does not exceed a predefined threshold. This threshold can be defined by simulating changing acceleration conditions and is presented in Section IV.A.

B. Formulation of the Proposed Attitude Estimation Algorithms

After the calibration routines are in place, it is possible to develop the estimation algorithm for attitude propagation. The aim of a computationally efficient algorithm is to improve the attitude accuracy of the LCT between two successive updates from the satellite's ADCS [21]. Two estimation strategies have then been considered and will be presented in the following. The algorithms will use the attitude information, in the form of quaternions, from the attitude estimation system and either the measurements from the LCT's sensor or internal propagation to provide accurate attitude knowledge at high sampling rates.

For the following example in Section IV, it is assumed that the satellite ADCS operates at 1 Hz while the LCT terminal has a sampling frequency of 200 Hz to account for higher frequency disturbances like micro-vibration and body-pointing drift. According to these rates, the estimated quaternion vector, representing the attitude of the LCT, is updated every 1 s with the estimated value of the quaternion vector of the ADCS knowledge $\hat{\mathbf{q}}_{\text{ADCS}}$. In between updates, the algorithms estimate the attitude of the LCT, using either linear extrapolation or quaternion kinematics propagation. The first proposed strategy relies only on the attitude information given by the ADCS updates. The latter algorithm

applies also the additional LCT gyroscope sensor measurements.

As first approach, a linear extrapolation of the quaternions in between the ADCS updates at the LCT's sampling rate of 200 Hz is pursued. As shown Equation 4, this algorithm performs the extrapolation of the predicted quaternion vector $\hat{\mathbf{q}}_{\text{extrap}}$ by deriving it according to a linear model from the two previously computed quaternions, with a step size of 5 ms. Meanwhile, every second the value of $\hat{\mathbf{q}}_{\text{extrap}}$ is reset to the attitude information $\hat{\mathbf{q}}_{\text{ADCS}}$, broadcasted by the satellite.

Since linear extrapolation does not preserve the unit norm of the quaternion, the estimate is renormalized as in Equation 5

$$\hat{\mathbf{q}}_{\text{extrap}}(t_k + n\Delta t) = \hat{\mathbf{q}}_{\text{ADCS}}(t_k) + \frac{n\Delta t}{t_k - t_{k-1}} \left(\hat{\mathbf{q}}_{\text{ADCS}}(t_k) - \hat{\mathbf{q}}_{\text{ADCS}}(t_{k-1}) \right) \quad (4)$$

where $\Delta t = 5 \text{ ms}$, $n = 1, 2, \dots, 200$

$$\hat{\mathbf{q}}_{\text{extrap}}(t_k + n\Delta t) \leftarrow \frac{\hat{\mathbf{q}}_{\text{extrap}}(t_k + n\Delta t)}{\|\hat{\mathbf{q}}_{\text{extrap}}(t_k + n\Delta t)\|} \quad (5)$$

The other proposed algorithm relies on the propagation of the quaternions by discrete-time integration of their kinematics [22] as shown in Equation 6

$$\dot{\mathbf{q}}(t) = \frac{1}{2} \Xi[\mathbf{q}(t)] \boldsymbol{\omega}(t), \quad (6)$$

where $\boldsymbol{\omega} \in \mathbb{R}^{3 \times 1}$ is the angular velocity vector and the quaternions matrix $\Xi(\mathbf{q}(t))$ is computed from the quaternions cross product $[\mathbf{q}_{1:3}]_{\times}$ as follows [22]

$$\Xi(\mathbf{q}(t)) \equiv \begin{bmatrix} q_4 I_{3 \times 3} + [\mathbf{q}_{1:3}]_{\times} \\ -\mathbf{q}_{1:3}^T \end{bmatrix} = \begin{bmatrix} q_4 & -q_3 & q_2 \\ q_3 & q_4 & -q_1 \\ -q_2 & q_1 & q_4 \\ -q_1 & -q_2 & -q_3 \end{bmatrix}. \quad (7)$$

Contrarily to the linear extrapolation method, the quaternions are estimated by exploiting their own kinematics law instead of making use of a pure mathematical linear relation. With this approach it is possible to take into account the natural time evolution of the considered quaternions and to combine it with the information coming from the angular velocity estimates of the ADCS. The proposed propagation, referred to as quaternion propagation, exploits also the LCT measurements for the discrete-time integration. Indeed, it uses the satellite updates $\hat{\mathbf{q}}_{\text{ADCS}}$ and the angular velocity $\tilde{\boldsymbol{\omega}}_{\text{gyro}}$ measured from the MEMS gyroscope sensor in $\dot{\mathbf{q}}(t) = \frac{1}{2} \Xi[\mathbf{q}(t)] \boldsymbol{\omega}(t)$. The algorithm scheme is illustrated in Figure 3. The propagation $\hat{\mathbf{q}}_{\text{prop,LCT}}$ occurs at a higher frequency of 200 Hz, as result of the integration $1/s$ of the

gyroscope measurements $\hat{\phi}_{\text{gyro}}$ and the error drift is kept bounded thanks to the ADCS quaternions periodically received at 1 Hz. The flow chart also includes the online calibration method described by Equations 2 and 3, which discards measurements indicated by the saturation symbol after the Laplace variable s beyond a set velocity threshold to ensure the quality of the online calibration.

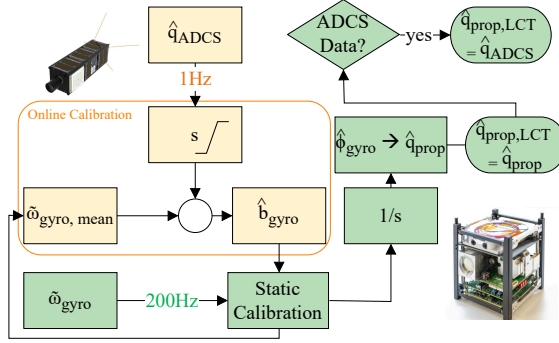


Fig. 3 Quaternion propagation algorithm scheme to fuse data from the ADCS and the LCT's gyroscope sensor, sampled at 1 Hz (orange) and 200 Hz (green) respectively.

C. Feed-Forward Fine Steering Mirror Control

Figure 4 illustrates how the estimated quaternions are transformed to control the FSM. It starts with the attitude knowledge of the LCT and ends at the required driving command voltage to achieve the necessary optical compensation angle.

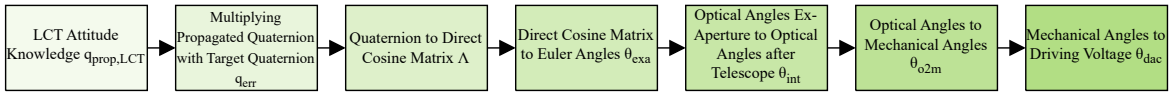


Fig. 4 Transformation from derived attitude quaternions to FSM control command voltage.

At first, the pointing error is determined by multiplying the propagated quaternion with the target quaternion to retrieve the pointing error quaternion $\mathbf{q}_{\text{err}} = \hat{\mathbf{q}} \otimes \bar{\mathbf{q}}$. The details of this operation are reported in Appendix V.A. The attitude matrix Λ of the LCT in the hexapod reference frame is derived from the quaternions [22] according to Equation 8

$$\Lambda(\mathbf{q}_{\text{err}}) = \begin{bmatrix} q_1^2 - q_2^2 - q_3^2 + q_4^2 & 2(q_1q_2 + q_3q_4) & 2(q_1q_3 - q_2q_4) \\ 2(q_2q_1 - q_3q_4) & -q_1^2 + q_2^2 - q_3^2 + q_4^2 & 2(q_2q_3 + q_1q_4) \\ 2(q_3q_1 + q_2q_4) & 2(q_3q_2 - q_1q_4) & -q_1^2 - q_2^2 + q_3^2 + q_4^2 \end{bmatrix}. \quad (8)$$

Afterwards, from the obtained direct cosine matrix, the sequence $\{\theta_x^3, \theta_y^2, \theta_z^1\}$ of hexapod Euler angles is computed [22]

as

$$\begin{cases} \theta_{x,\text{hxp}} = \text{atan2}\left(2(q_2q_3 + q_1q_4), 1 - 2(q_1^2 + q_2^2)\right) = \text{atan2}([\Lambda]_{23}, [\Lambda]_{33}) \\ \theta_{y,\text{hxp}} = \arcsin(-2(q_1q_3 - q_2q_4)) = \sin^{-1}(-[\Lambda]_{13}) \\ \theta_{z,\text{hxp}} = \text{atan2}\left(2(q_1q_2 + q_3q_4), 1 - 2(q_2^2 + q_3^2)\right) = \text{atan2}([\Lambda]_{12}, [\Lambda]_{11}) \end{cases} \quad (9)$$

Comparing the reference frames of the FSM and of the hexapod illustrated in Figure 5, it is noticeable that a rotation around $\theta_{x,\text{fsm}}$ corresponds to a rotation around $\theta_{z,\text{hxp}}$ and analogously $\theta_{y,\text{fsm}}$ to $\theta_{y,\text{hxp}}$ as well as $\theta_{z,\text{fsm}}$ to $-\theta_{x,\text{hxp}}$. Equally expressed by

$$\theta_{x,\text{fsm}} = \theta_{z,\text{hxp}}, \quad \theta_{y,\text{fsm}} = \theta_{y,\text{hxp}}, \quad \theta_{z,\text{fsm}} = -\theta_{x,\text{hxp}}, \quad (10)$$

where the FSM angle around the third axis has been canceled because rotations around the laser pointing direction axis do not affect the pointing. The known pointing error is therefore given in the FSM reference frame. However, to

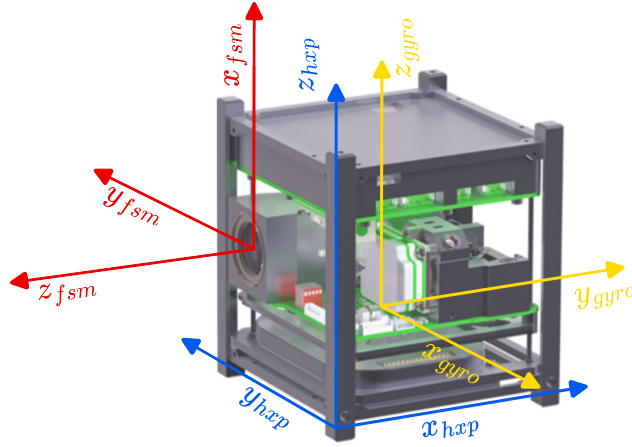


Fig. 5 Reference frames of the FSM(—), satellite/hexapod(—), and gyroscope sensor(—) in the example of the CubeISL payload [16].

command a corresponding voltage to the FSM control voltage in a feed-forward manner, it is necessary to convert from the optical domain ex-aperture via the internal optical domain after the compression telescope to the mechanical domain and finally to the electrical domain as follows: $\theta_{x/y,\text{exa}} \rightarrow \theta_{x/y,\text{int}} \rightarrow \theta_{x/y,\text{o2m}} \rightarrow \theta_{x/y,\text{dac}}$, where $\theta_{x/y,\text{exa}} = \theta_{x/y,\text{fsm}}$. In a first step the conversion accounting for the telescope magnification $M_{\text{telescope}}$ is performed using Equation 11

$$\theta_{x/y,\text{int}} = \theta_{x/y,\text{exa}} \cdot M_{\text{telescope}}. \quad (11)$$

In the following, the conversion from the optical to the mechanical domain needs to be performed. In general, an optical beam is reflected with the same angle as the angle of incidence, therefore doubling the mechanical deflection that is used for compensation. However, because the FSM is often mounted at a 45 degree angle with respect to the incoming

beam, in many optical designs, three-dimensional angle contemplation is necessary. Due to the coupled axis, a rotation of the mirror

$$\begin{aligned} \theta_{x,int} = & \arcsin \left(2 \sin \left(2 \theta_{x,stat} \right) \cos \left(\theta_{x,o2m} \right)^2 \cos \left(\theta_{y,o2m} \right)^2 \right. \\ & + 2 \cos \left(2 \theta_{x,stat} \right) \sin \left(\theta_{x,o2m} \right) \cos \left(\theta_{x,o2m} \right) \cos \left(\theta_{y,o2m} \right)^2 \\ & \left. - \sin \left(2 \theta_{x,stat} \right) \right) \end{aligned} \quad (12)$$

has to be treated with respect to the FSM inertial system. Due to the 45 degree static mounting angle θ_{stat} however, Equation 12 simplifies to

$$\theta_{x,int} = \arcsin \left(2 \cos \left(\theta_{x,o2m} \right)^2 \cos \left(\theta_{y,o2m} \right)^2 - 1 \right), \quad (13)$$

while the other axis is independent of the static angle

$$\theta_{y,int} = \arcsin \left(2 \cos \left(\theta_{x,o2m} \right) \cos \left(\theta_{y,o2m} \right) \sin \left(\theta_{y,o2m} \right) \right). \quad (14)$$

Equation 14 can then be solved for

$$\theta_{x,o2m} = \arccos \left(\frac{\sin \left(\theta_{y,int} \right)}{2 \cos \left(\theta_{y,o2m} \right) \sin \left(\theta_{y,o2m} \right)} \right), \quad (15)$$

which however still depends on the results of $\theta_{y,o2m}$. Therefore, when Equation 15 is used as a substitute for $\theta_{x,o2m}$ in Equation 13, $\theta_{y,o2m}$ can be retrieved after rearrangement

$$\theta_{y,o2m} = \arcsin \left(\frac{\sin \left(\theta_{y,int} \right)}{\sqrt{2 + 2 \sin \left(\theta_{x,int} \right)}} \right). \quad (16)$$

As a final step, Equation 16 can be inserted into Equation 15 and yields after simplification

$$\theta_{x,o2m} = \arccos \left(\frac{\sqrt{2 + 2 \sin \left(\theta_{x,int} \right)}}{2 \sqrt{1 - \frac{\sin \left(\theta_{y,int} \right)^2}{2 + 2 \sin \left(\theta_{x,int} \right)}}} \right). \quad (17)$$

With both mechanical angles at hand, the command voltage for the specific device needs to be retrieved. Since the FSM is driven in an open-loop manner during acquisition and the MEMS FSM is characterized by a non-linear relationship between angle and voltage [23], the command is approximated by a third order polynomial of the form

$$\theta_{x/y,dac} = a_0 + a_1 \cdot \theta_{x/y,o2m} + a_2 \cdot \theta_{x/y,o2m}^2 + a_3 \cdot \theta_{x/y,o2m}^3. \quad (18)$$

This transformation and its coefficients need to be adapted to the specific MEMS FSM and electronics in use.

IV. Validation of the Pointing Stability Compensation Algorithm

In this section, the results of the proposed propagation algorithms are presented and discussed. Based on a simulation model, all relevant methods can be compared under controlled conditions. This evaluation is the basis for the implementation of the propagation used for hardware validation. It demonstrates the advantages of the proposed concept and explores the limits for its application. Therefore, after a calibration and validation campaign, the final performance is evaluated on a hardware-in-the-loop testbed.

A. Simulation Analysis of the Attitude Knowledge Performance

The algorithms have been implemented in a Simulink environment to analyze their performance and to quantify the improvement obtained by using the additional attitude information from the LCT at 200 Hz compared to considering only the attitude updates received periodically from the satellite at 1 Hz.

For simulation purposes, reference attitude parameters have been created to represent the attitude of the satellite platform. The components of the satellite angular velocity ω_{ADCS} are implemented as damped sinusoidal function

$$\omega(t) = G \cdot e^{-d \cdot t} \cdot \sin(f \cdot t + \Phi), \quad (19)$$

with initial amplitude gain G of 0.2 rad s^{-1} , f of 0.1 rad s^{-1} and Φ of $[0, 5, -5]$ rad respectively for the three body axes and a damping coefficient d of 0.01. The reference angular velocity is dampened in order to simulate two different mission scenarios. The first scenario is a dynamic maneuver that occurs in the first half of the simulation. This is followed by a more stable attitude, which is similar to the tracking phase in the second half of the simulation.

The reference quaternion vector \mathbf{q}_{ADCS} is then retrieved from the angular velocity according to the quaternion kinematics equation with initial conditions $\mathbf{q}_{\text{ADCS},0} = [0; 0; 0; 1]$ and a simulation sampling rate of $1 \cdot 10^{-4}$ s. This attitude data represents the real reference quaternion of the simulation and is the input to the LCT to perform its own attitude propagation. The model of the gyroscope sensor is derived according to the data sheet (IAM20380, TDK InvenSense [24]), considering a natural frequency of 1000 Hz and a cut-off frequency of 177 Hz. The characteristic noise power of $0.02^2 \text{ dps}^2/\text{Hz}$ was measured on the test hardware.

The simulation runs for 800 s, which allows enough time to evaluate the dynamic maneuver and tracking scenario. To quantify the estimation errors of the presented methods, an analysis of the attitude error vector $\boldsymbol{\varepsilon}$ in the body frame is performed to compute the pointing errors resulting from the estimation algorithms themselves. To achieve this, the estimated $\hat{\Lambda}$ and the actual Λ_{ADCS} posture matrices are first derived from $\hat{\mathbf{q}}$ and \mathbf{q}_{ADCS} , respectively, according to equation 8 but using the estimated quaternion instead of the error quaternion. Next, the attitude error matrix $\tilde{\Lambda}$ is computed as in Equation 20, and the attitude error vector is actually extracted from its components according to the

small-angles approximation [22] as $\boldsymbol{\varepsilon} = [\tilde{\Lambda}_{23}; \tilde{\Lambda}_{31}; \tilde{\Lambda}_{12}]$

$$\tilde{\Lambda} = \hat{\Lambda} \Lambda_{\text{ADCS}}^T. \quad (20)$$

Moreover, the pointing error α is computed for both methods, as the angle between the true direction and the estimated direction. By selecting the spacecraft boresight direction $\mathbf{r} = [0; 0; 1]$ as the desired target direction in the inertial frame, the reference true direction \mathbf{u}_{true} and the estimated direction $\hat{\mathbf{u}}$ in the body frame are respectively obtained as:

$$\mathbf{u}_{\text{true}} = \Lambda_{\text{ADCS}} \mathbf{r}, \quad \hat{\mathbf{u}} = \hat{\Lambda} \mathbf{r} \quad (21)$$

Indeed, the pointing error α is retrieved according to Equation 22 and then converted from radians to degrees [22].

$$\alpha = \cos^{-1}(\mathbf{u}_{\text{true}}^\top \hat{\mathbf{u}}) \quad (22)$$

To compare the algorithms, the root mean square error (RMSE) of $\boldsymbol{\varepsilon}$ and α are computed for the entire simulation time span (here referred as "Full simulation"), for the first 400 s (the "Dynamic scenario") and over the last part of the simulation (referred as "Tracking scenario"). Subsequently, the vectorial norm of the components of the obtained $RMSE_{\boldsymbol{\varepsilon}}$ is taken, resulting in $\|RMSE_{\boldsymbol{\varepsilon}}\|$. The temporal division of the simulation is performed to highlight the performance of the algorithms in presence of a dynamic maneuver, characterized by a maximum angular acceleration outside of $\pm 0.023 \text{ deg s}^{-2}$ in the initial segment of the simulation, and during a more stable attitude exhibiting a maximum angular acceleration within $\pm 0.023 \text{ deg s}^{-2}$, which resembles the tracking phase in the subsequent segment. The computed errors are collected in Table 2, where $\|RMSE_{\boldsymbol{\varepsilon}}\|$ represents the error derived from the estimation process itself for each algorithm, while $RMSE_{\alpha}$ gives the physical pointing error angle. As expected, the RMSE of the pointing error angle results to be lower than the norm of the RMSE of the attitude error vector for the each scenario, being the instantaneous angular misalignment upper bounded by the attitude error magnitude [22].

Table 2 Performance parameters of the attitude estimation algorithms over the Full Simulation and for the Dynamic and Tracking scenarios

| Algorithm | $\ RMSE_{\boldsymbol{\varepsilon}}\ , \text{ deg}$ | | | $RMSE_{\alpha}, \text{ deg}$ | | |
|------------------------|--|---------|----------|------------------------------|---------|----------|
| | Full Sim | Dynamic | Tracking | Full Sim | Dynamic | Tracking |
| Linear extrapolation | 0.3234 | 0.5114 | 0.0046 | 0.2349 | 0.3714 | 0.0035 |
| Quaternion propagation | 0.0262 | 0.0282 | 0.0248 | 0.0211 | 0.0226 | 0.0203 |

The results of the entire simulation indicate that the quaternion propagation algorithm exhibits superior performance

in comparison to the linear extrapolation. This observation is supported by the estimation errors for both $\|RMSE_{\epsilon}\|$ and $RMSE_{\alpha}$ with respect to the actual attitude of the ADCS satellite.

In the initial phases of the simulation, referred to as the dynamic phase, when the satellite angular velocity and angular acceleration are at their peak and the platform is undergoing significant movements, it becomes evident that the proposed quaternion propagation method, leveraging the LCT information, yields reduced errors in comparison to the linear extrapolation. This superior performance can be attributed to the fact that, in scenarios where attitudes undergo rapid and substantial changes, a linear function for extrapolation may be inadequate due to the non-linear nature of the quantities being estimated. Moreover, the rapid fluctuations in the angular rate result in substantial variations in the attitude between successive updates.

Instead, the second part of the simulation can be considered as the tracking phase, during which the satellite maintains a stable attitude with respect to the Earth's center, while the attitude parameters undergo gradual changes in their absolute values. In this scenario, the linear extrapolation performs better. However, the performance of the quaternion propagation is hindered by the presence of noise, which affects the estimation through integration from the MEMS gyroscope sensor measurements. This noise imposes limitations on the minimum attainable estimation error, resulting in elevated errors for both the attitude error and the pointing error when compared to the errors obtained by the alternative method that do not utilize gyroscope sensor measurements.

Overall, it has been already demonstrated that the presence of any estimation process performed by the LCT, at higher rates with respect to the satellite ADCS's one, leads to a significant improvement in the attitude knowledge between satellite updates with respect to rely only on the information of the ADCS itself [25]. Nonetheless, the calculation of the next update based only on past measurements by linear extrapolation proved to be not accurate when the attitude values change non-linearly due to e.g. a non-zero jerk in the acceleration profile. On the contrary, it was found that quaternion propagation algorithms can lead to a better attitude estimation until the lower limit of 0.4 deg s^{-1} for the sinusoidal amplitude of Equation 19, corresponding to an angular acceleration of more or equal than 0.04 deg s^{-2} , after which this strategy should be employed with care.

B. Hardware Validation Measurements

The testing setup, which comprises the necessary measurement and emulation equipment contains the following devices. A telescope tube, referred to as the optical ground support equipment, simulates the beam emitted by an OGS as it would be received by the LCT in space. Further, it modulates the beacon signal with the same 10 kHz modulation frequency which is used to distinguish it from any background light. The LCT itself is mounted on a hexapod (HXP50-MECA, Newport), that can be precisely manipulated in all six degrees of freedom and controlled to mimic the behavior of the spacecraft. The tracking laser can be observed by an infrared camera, which serves as a reference to evaluate the performance of the algorithm.

To verify the performance of the estimation algorithm, the sensors must be calibrated first as previously discussed in Section III.A. On the LCT this concerns the MEMS gyroscope sensor and the MEMS FSM, which is coupled to the attitude of the satellite via the optical system. In both cases, the calibrated coordinate system of the ADCS, which is represented by the hexapod in the test, serves as a reference. In addition, the online bias compensation implementation is verified during a temperature cycle test.

1. Static Calibration for Device and Assembly Errors

In the test setup, the terminal is rotated on a turntable at multiple speeds around each axis. The used test runs include 15 deg s^{-1} , -10 deg s^{-1} , 5 deg s^{-1} , -2.5 deg s^{-1} , 1.25 deg s^{-1} and -10 deg s^{-1} in that order, where each procedure is performed for approximately 10 s to 20 s. The last movement with -10 deg s^{-1} is used to finish the procedure at the starting point of the turntable. This ensures that the algorithm does not overfit the calibration parameters to one particular motion that is performed during the calibration process on-orbit. The following calibration gain error matrix and offset for static calibration were obtained from the measurements according to Equation 2.

$$\mathbf{C} = \begin{bmatrix} 1.0008 & -0.0264 & 0.0184 \\ 0.0256 & 1.0052 & -0.0111 \\ -0.0556 & -0.0481 & -1.0066 \end{bmatrix}, \quad \mathbf{b} = \begin{bmatrix} 0.35 \\ -2.69 \\ 0.28 \end{bmatrix}. \quad (23)$$

Mounting the LCT into the satellite is limited to mechanical tolerances which impose deviations compared to the computer aided design (CAD) coordinate frame. These variations can be accounted for by recording tracking data which contain mirror movements as well as gyroscope sensor measurements using an LSM similar to the initial static calibration but assuming the sensor is already pre-calibrated. The remaining error should therefore only consist of coordinate rotations. Since the FSM has only two degrees of freedom and the gyroscope sensor measures in all three dimensions, the resulting rotation matrix is of size $\mathbf{R}_{\text{est}} \in \mathbb{R}^{3 \times 2}$.

$$\hat{\omega}_{\text{gyro}}^{3 \times 1} = \mathbf{R}_{\text{est}}^{3 \times 2} \cdot \omega_{\text{FSM}}^{2 \times 1} \quad (24)$$

The CAD model contains the theoretical rotation matrix between the gyroscope sensor, calibrated to the FSM frame, and the satellite's ADCS reference frame. Therefore, any deviation of the mounting orientation will be visible by comparing the rotation matrix \mathbf{R}_{est} obtained from FSM calibrated gyroscope sensor measurements with the theoretical

rotation matrix \mathbf{R}_{CAD} . The following results indicate a deviation from the ideal orientation.

$$\mathbf{R}_{est} = \begin{bmatrix} 0.046 & 0.992 \\ 0.019 & -0.059 \\ 0.960 & -0.044 \end{bmatrix}, \quad \mathbf{R}_{CAD} = \begin{bmatrix} 0 & 0 & -1 \\ 0 & -1 & 0 \\ -1 & 0 & 0 \end{bmatrix}. \quad (25)$$

To validate the reconstruction of mounting errors, simulated data is purposely rotated and then compared with the original simulated data to determine the exact rotation parameters. Note that in order to model the real scenario of three gyroscope axes and two FSM axes, a matrix $\mathbf{R}_{est} \in \mathbb{R}^{3 \times 2}$ has been estimated from the simulated data. By calculating the cross-product between the two column vectors making up \mathbf{R}_{est} , a third, perpendicular column vector emerges.

$$\mathbf{R}_{est,\perp} = \mathbf{R}_{est,1} \times \mathbf{R}_{est,2}, \quad \mathbb{R}_{est,3D} = [\mathbf{R}_{est,1}, \mathbf{R}_{est,2}, \mathbf{R}_{est,\perp}] \quad (26)$$

This vector is appended to the matrix to form $\mathbf{R}_{est,3D} \in \mathbb{R}^{3 \times 3}$, from which the angles can be determined. The sensor model used for the simulation is adapted from previous work [26] with added quantization, saturation and erroneous influences such as scaling error, bias and noise. Table 3 shows the angles set in the simulation and the reconstructed angular deviation with α , β and γ corresponding to a rotation around the x, y and z axis in this order of the gyroscope sensor according to Figure 5 respectively.

Table 3 Comparison of real and reconstructed rotation angles with simulated data. Reconstruction is obtained from two axes of simulated data and a calculated perpendicular vector.

| | $\alpha_{x, \text{gyro, deg}}$ | $\beta_{y, \text{gyro, deg}}$ | $\gamma_{z, \text{gyro, deg}}$ |
|----------------------|--------------------------------|-------------------------------|--------------------------------|
| Real Angle | 30 | 75 | 130 |
| Reconstructed | 29.992 | 75.007 | 130.015 |
| Difference | 0.008 | 0.007 | -0.015 |

It can be seen that an accuracy of 15 mdeg or lower can be achieved.

2. Online Gyroscope Sensor Calibration during Dynamic Temperature Variations

The satellite will frequently experience temperature changes as it moves inside and outside of eclipse zones, which may lead to bias drifts. Keeping track of these drifts is essential to maintain a good propagation quality. Instead of using a pre-calibrated temperature curve, the presented online bias estimation algorithm should be used to account for any deviation. To test the robustness of the online gyroscope sensor calibration algorithm to temperature changes, a hot air gun was used to heat the gyroscope sensor to approximately 50 °C.

Figure 6 presents the results of an experiment where the hexapod remained stationary throughout, isolating temperature-induced effects. In Figure 6a, noticeable shifts in estimated biases occur during the active heating and

following cooling phase, where the gyroscope sensor was allowed time to return to ambient temperature. Figure 6b demonstrates that the algorithm works effectively as the calibrated angular rates are close to a zero rate as expected. Note that the spikes are single sample outliers from the measurement.

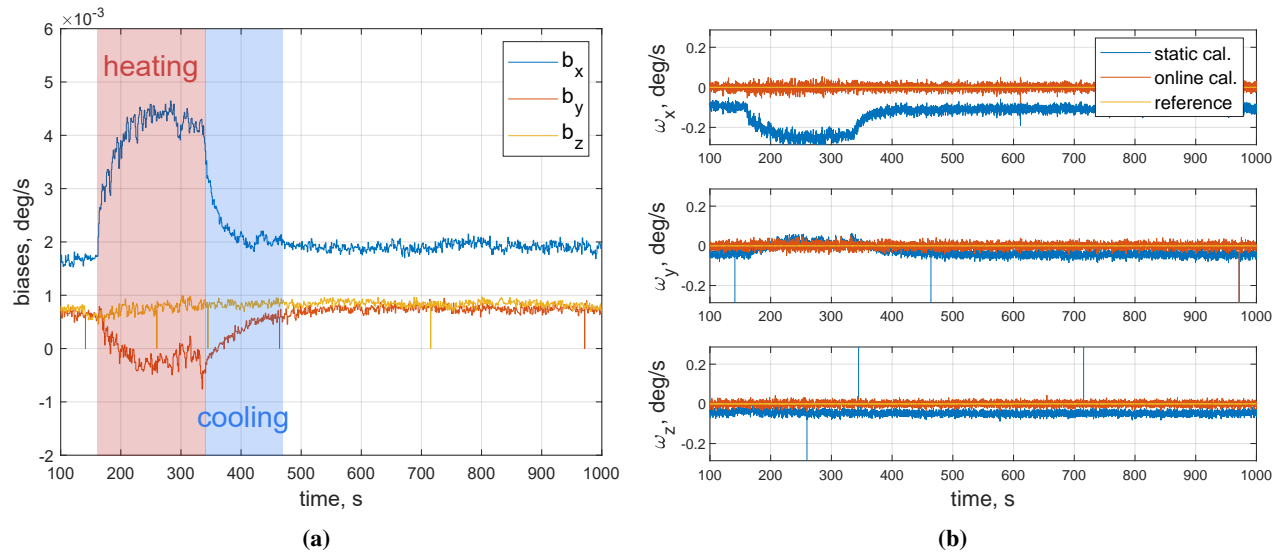


Fig. 6 (a) Bias online estimation during temperature changes and (b) comparison between an online and a statically calibrated gyroscope sensor during temperature changes.

C. Hardware Attitude Knowledge Performance

The highly accurate encoders of the hexapod, integrated into the actuators, enabled the retrieval of a reference attitude, which was then used to assess the precision of the attitude propagation algorithm depicted in Figure 3. The hexapod is commanded through a Python interface containing the relevant software drivers. This interface provides real-time readings of its attitude, which are fed to the CubeISL microcontroller via a serial interface to simulate the propagation reset with the estimated quaternions of the satellite ADCS.

1. Gyroscope Sensor Based Attitude Propagation

Table 4 illustrates the absolute error values in Euler angles for various propagation strategies, with resets occurring at 1 Hz. It presents the statistical results from the specific test and highlights the benefits of recursively calibrating the gyroscope sensor. The linear extrapolation condition refers to the scenario where attitude is linearly extrapolated between ADCS estimates. The quaternion propagation refers to the case with the LCT gyroscope sensor involved. The online-limited method also accounts for scenarios where high accelerations would distort the online calibration and related measurements are therefore automatically discarded.

Similar to the simulations, Case 1 represents a scenario with slowly changing velocities comparable to the aforementioned tracking phase. Here the linear extrapolation achieves comparable results with respect to the online

Table 4 The error statistics definition of the linear extrapolation and quaternion propagation methods are as follows: linear propagation uses no measurements, while quaternion propagation uses internal gyroscope measurements. "Static" means only static calibration is applied, while "online" calibration is used with or without velocity limitations of the calibration reference.

| | μ_{θ} , deg | σ_{θ} , deg |
|--|----------------------|-------------------------|
| Case 1: Linear extrapolation | 0.0079 | 0.0141 |
| Case 1: Quaternion propagation (Static) | 0.0200 | 0.0269 |
| Case 1: Quaternion propagation (Online) | 0.0091 | 0.0153 |
| Case 2: Linear extrapolation | 0.7322 | 0.8533 |
| Case 2: Quaternion propagation (Online) | 0.7003 | 0.8935 |
| Case 2: Quaternion propagation (Online-Limited) | 0.3625 | 0.4640 |

calibrated quaternion propagation. However, in the dynamic scenario of Case 2 the online-limited quaternion propagation clearly outperforms the linear extrapolation. In duration with low dynamics the online bias estimation has its largest effect and can therefore be specifically used during those maneuvers, adding to the performance within accelerated rotations.

2. Feed-Forward Pointing Stability Compensation

Finally, the gained attitude knowledge of the LCT shall be used to compensate for the known pointing instabilities and drifts of the host platform. Therefore, hardware-in-the-loop tests using CubeISL are conducted to demonstrate that the FSM control with attitude information can augment the attitude knowledge and therefore reduce the acquisition time (see Fig. 7b). In Figure 7a an example of propagated offset angles due to body-pointing drift is depicted, showing how reference updates from the ADCS at every second only have minor effects on the propagation and, therefore, the commanding of the FSM.

The hexapod's initial position was set to simulate the scenario in which the received laser spot is at the center of the QPD, which resembles zero error body-pointing. Dynamic maneuvers within 1 deg and with 0.1 deg s^{-1} angular velocity and 0.4 deg s^{-2} angular acceleration are executed. These values represent the maximum field of regard offered by the FSM and the highest expected drift rate, respectively. In this way it is directly visible whether the LCT is able to stay within the FOV of its tracking sensor.

The results substantiate that, during the experiment, the laser remained within the FOV of the QPD for 63.3% of the time, meaning that the sum of the signal voltage exceeds the identified tracking threshold. This result shows that the compensation algorithm does not always compensate the drift within the FOV, which can be explained by slight errors within the calibration and feed-forward path as well as measurement inaccuracies. However, as explained in the beginning, a search pattern will be superposed to the compensation. This means that remaining errors can be overcome. As a result of the active drift compensation, the pattern can be executed in a much smaller area, therefore increasing the success probability of link acquisition and reducing the expected time needed. This outcome confirms that using

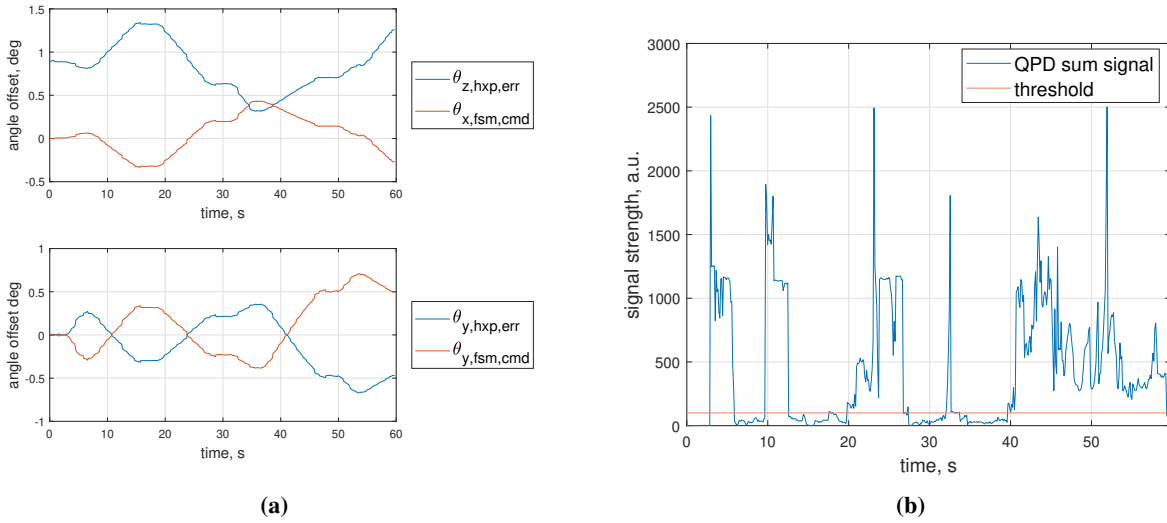


Fig. 7 (a) Data of a quaternion propagated offset angle with feed-forward compensation commands to the FSM and (b) sum of the QPD power sum signal with respect to the acquisition threshold as 16-bit integer values.

feed-forward compensation, the laser terminal can compensate body pointing errors, allowing for increased acquisition performance due to a reduced FOU.

V. Conclusion

This study presents a feed-forward compensation approach that enhances the pointing accuracy of LCTs by integrating ADCS data with onboard gyroscope sensor measurements. By mitigating body-pointing uncertainties, the proposed method significantly improves the optical link acquisition process by mitigating satellite pointing errors using feed-forward compensation of the FSM, increasing the probability of successful link establishment while reducing acquisition time. In summary, the proposed methods are defined as follows: the linear extrapolation method does not use any measurements, whereas the quaternion propagation method uses measurements from internal gyroscopes. "Static" refers to calibration applied only once and remaining fixed, while "online" refers to continuous calibration, which may or may not include velocity limits for the calibration reference.

Hardware-in-the-loop validation and simulations demonstrate that quaternion propagation using gyroscopic data outperforms linear extrapolation, particularly in dynamic scenarios as in Case 2. In Case 1 (the low-dynamic tracking phase), where angular velocity changes gradually, both methods perform similarly. Quaternion propagation, which uses online calibration, achieves a mean error of 0.0091 degrees and a standard deviation of 0.0153 degrees. This is slightly higher than the mean error of 0.0079 degrees and standard deviation of 0.0141 degrees achieved by linear extrapolation. However, in Case 2 (high-dynamic scenario), where the satellite experiences rapid angular acceleration, quaternion propagation with an online-limited calibration achieves a mean error of 0.3625 degrees and a standard deviation of 0.4640 degrees, significantly outperforming linear extrapolation, which exhibits a mean error of 0.7322 degrees and

a standard deviation of 0.8533 degrees. This represents a 50% improvement in mean error and a 45% reduction in pointing uncertainty under dynamic conditions.

The proposed method also provides an effective FOU reduction within ± 0.2 degrees, ensuring that the FSM maintains optical alignment during acquisition even in the presence of body-pointing disturbances. Additionally, the online bias calibration technique successfully compensates for gyroscope sensor drift due to temperature variations, maintaining stable performance in varying environmental conditions. As an added benefit, pre- and post-launch calibration can be used to detect any launch-related misalignment between the FSM and ADCS frames.

A key advantage of this approach is its ability to enhance pointing precision without requiring additional optical feedback during acquisition, making it highly suitable for CubeSats with size, weight, and power constraints. However, at angular accelerations below 0.04 deg s^{-2} , gyroscope sensor noise and calibration errors start to degrade performance, limiting its applicability in low dynamic scenarios such that linear extrapolation is preferred.

Appendix

A. Quaternion Multiplication

As noted in [22], quaternion multiplication can be expressed using matrix operations, analogous to the vector cross product:

$$\mathbf{q} \otimes \bar{\mathbf{q}} = [\mathbf{q} \otimes] \bar{\mathbf{q}} = \bar{\mathbf{q}} \odot \mathbf{q}, \quad (27a)$$

$$\mathbf{q} \odot \bar{\mathbf{q}} = [\mathbf{q} \odot] \bar{\mathbf{q}} = \bar{\mathbf{q}} \otimes \mathbf{q}, \quad (27b)$$

where

$$[\mathbf{q} \otimes] \equiv \begin{bmatrix} q_4 I_{3 \times 3} - [\mathbf{q}_{1:3}]_{\times} & \mathbf{q}_{1:3} \\ -\mathbf{q}_{1:3}^T & q_4 \end{bmatrix} = \begin{bmatrix} \Psi(\mathbf{q}) & \mathbf{q} \end{bmatrix}, \quad (28)$$

and

$$[\mathbf{q} \odot] \equiv \begin{bmatrix} q_4 I_{3 \times 3} + [\mathbf{q}_{1:3}]_{\times} & \mathbf{q}_{1:3} \\ -\mathbf{q}_{1:3}^T & q_4 \end{bmatrix} = \begin{bmatrix} \Xi(\mathbf{q}) & \mathbf{q} \end{bmatrix}, \quad (29)$$

with $\Psi(\mathbf{q})$ and $\Xi(\mathbf{q})$ being the 4×3 matrices

$$\Psi(\mathbf{q}) \equiv \begin{bmatrix} q_4 I_{3 \times 3} - [\mathbf{q}_{1:3}]_{\times} \\ -\mathbf{q}_{1:3}^T \end{bmatrix} = \begin{bmatrix} q_4 & q_3 & -q_2 \\ -q_3 & q_4 & q_1 \\ q_2 & -q_1 & q_4 \\ -q_1 & -q_2 & -q_3 \end{bmatrix}, \quad (30)$$

and

$$\Xi(\mathbf{q}) \equiv \begin{bmatrix} q_4 I_{3 \times 3} + [\mathbf{q}_{1:3}]_{\times} \\ -\mathbf{q}_{1:3}^T \end{bmatrix} = \begin{bmatrix} q_4 & -q_3 & q_2 \\ q_3 & q_4 & -q_1 \\ -q_2 & q_1 & q_4 \\ -q_1 & -q_2 & -q_3 \end{bmatrix}. \quad (31)$$

Funding Sources

This research work is supported by the German Federal Ministry of Defense through the technological research and development assignment ‘‘Responsive Space Capabilities’’.

Acknowledgements

The TDK InvenSense sensors described in this publication were not designed, tested, or qualified for aerospace use. TDK InvenSense makes no representations or warranties regarding their suitability, reliability, or performance in such environments. Any use of these products in aerospace applications is entirely at the user’s own risk. TDK InvenSense does not object to the research use of these products as described in this publication, but this does not constitute an endorsement or recommendation of these products in aerospace or space applications.

During the preparation of this work, the authors used DeepL in order to improve the readability and language of the manuscript.

References

- [1] Weston, S. V., Burkhard, C. D., Stupl, J. M., Ticknor, R. L., Yost, B. D., Austin, R. A., Galchenko, P., Newman, L. K., and Santos Soto, L., ‘‘State-of-the-art small spacecraft technology,’’ NASA/TP NASA/TP—20250000142, National Aeronautics and Space Administration, Ames Research Center, Moffett Field, CA 94035-1000, February 2025. URL <https://www.nasa.gov/smallsat-institute/sst-soa/>.
- [2] Elsner, L., Petermann, T., von Arnim, M., and Schilling, K., ‘‘Pre-Flight Verification of the Cubesat Attitude Control System for

- the QUBE Mission,” The 4S Symposium 2024, 2024, p. 11. <https://doi.org/10.1117/12.3062785>.
- [3] Kingsbury, R., Riesing, K., and Cahoy, K., “Design of a free-space optical communication module for small satellites,” Proceedings of the Small Satellite Conference, 2014, p. 10. URL <https://digitalcommons.usu.edu/smallsat/2014/advtechcomm/6/>.
- [4] Agrawal, P. S., Fuller, C. O., Kung, K. R., and DiMatteo, J. J., “From Design to Orbit: Engineering Sub-Arcsecond CubeSat Pointing Performance on Pathfinder-3,” Proceedings of the Small Satellite Conference, 2024, p. 10. URL <https://digitalcommons.usu.edu/smallsat/2024/all2024/125/>.
- [5] Li, S., and Zhong, M., “High-Precision Disturbance Compensation for a Three-Axis Gyro-stabilized Camera Mount,” IEEE/ASME Transactions on Mechatronics, Vol. 20, No. 6, 2015, pp. 3135–3147. <https://doi.org/10.1109/TMECH.2015.2394456>.
- [6] Dell’Olio, F., Natale, T., Wang, Y.-C., and Hung, Y.-J., “Miniaturization of Interferometric Optical Gyroscopes: A Review,” IEEE Sensors Journal, Vol. 23, No. 24, 2023, pp. 29948–29968. <https://doi.org/10.1109/JSEN.2023.3327217>.
- [7] Heimann, M., Liesegang, M., Arndt-Staufenbiel, N., Schröder, H., and Lang, K.-D., “Optical system components for navigation grade fiber optic gyroscopes,” Emerging Technologies in Security and Defence; and Quantum Security II; and Unmanned Sensor Systems X, SPIE, 2013, p. 88991A. <https://doi.org/10.1117/12.2029097>.
- [8] Shukri, Z., Rezaei, H., Fasihaniyard, M., Ghofrani, S., Bissonnette, J., Gravey, T., Romanuik, S., Tewari, R., and Zandi, K., “Photonic integrated circuit microchip-based optical gyroscopes for high-precision inertial measurement units,” Integrated Optics: Devices, Materials, and Technologies XXIX, edited by S. M. García-Blanco and P. Cheben, SPIE, 25.01.2025 - 31.01.2025, p. 25. <https://doi.org/10.1117/12.3041353>.
- [9] Rüdtenklau, R., and Schitter, G., “Optimisation of acquisition patterns for establishing inter CubeSat optical communications,” Journal of Optical Communications and Networking, 2024. <https://doi.org/10.1364/JOCN.518004>.
- [10] AAC Clyde Space, “iADCS400,” , 2024. URL <https://www.aac-clyde.space/wp-content/uploads/2021/11/iADCS400-1.pdf>.
- [11] Alén Space, “6U Platform,” , 2024. URL <https://alen.space/products/6u-platform/>.
- [12] Blue Canyon, “XB6,” , 2024. URL https://storage.googleapis.com/blue-canyon-tech-news/1/2024/03/6U-1_2024.pdf.
- [13] Gomspace, “6U Premium,” , 2024. URL <https://gomspace.com/6u-premium.aspx>.
- [14] Nano Avionics, “M6P Max,” , 2024. URL <https://nanoavionics.com/small-satellite-buses/6u-cubesat-nanosatellite-m6p/>.
- [15] Rüdtenklau, R., Rein, F., Roubal, C., Rödiger, B., and Schmidt, C., “In-orbit demonstration of acquisition and tracking on OSIRIS4CubeSat,” Opt. Express, Vol. 32, No. 23, 2024, pp. 41188–41200. <https://doi.org/10.1364/OE.537889>, URL <https://opg.optica.org/oe/abstract.cfm?URI=oe-32-23-41188>.

- [16] Nonay, J. R., Rüdtenklau, R., Sinn, A., Jakobs, J. P., Berlitz, J., Rodiger, B., and Schitter, G., “Horizontal free-space optical link with CubeISL over 143 km,” Journal of Optical Communications and Networking, Vol. 16, No. 5, 2024, pp. 593–601. <https://doi.org/10.1364/JOCN.518271>.
- [17] Bangert, P., Busch, S., and Schilling, K., “In-orbit performance of the pico-satellite UWE-3,” , 2015. URL https://www.researchgate.net/profile/Stephan-Busch-4/publication/286379222_In-Orbit_Performance_of_the_Pico-Satellite_UWE-3/links/614f4faf522ef665fb5ec793/In-Orbit-Performance-of-the-Pico-Satellite-UWE-3.pdf.
- [18] Poddar, S., Kumar, V., and Kumar, A., “A comprehensive overview of inertial sensor calibration techniques,” Journal of Dynamic Systems, Measurement, and Control, Vol. 139, No. 1, 2017, p. 011006. <https://doi.org/10.1115/1.4034419>.
- [19] Springmann, J. C., and Cutler, J. W., “Attitude-independent magnetometer calibration with time-varying bias,” Journal of Guidance, Control, and Dynamics, Vol. 35, No. 4, 2012, pp. 1080–1088. <https://doi.org/10.2514/1.56726>.
- [20] Springmann, J. C., and Cutler, J. W., “Flight results of a low-cost attitude determination system,” Acta Astronautica, Vol. 99, 2014, pp. 201–214. <https://doi.org/10.1016/j.actaastro.2014.02.026>.
- [21] Wertz, J. R., Spacecraft attitude determination and control, Vol. 73, Springer Science & Business Media, 2012.
- [22] Markley, F Landis and Crassidis, John L, Correction to: Fundamentals of Spacecraft Attitude Determination and Control, Springer, 2014. <https://doi.org/10.1007/978-1-4939-0802-8>.
- [23] Milanovic, V., Matus, G. A., and McCormick, D. T., “Gimbal-Less Monolithic Silicon Actuators for Tip–Tilt–Piston Micromirror Applications,” IEEE Journal of Selected Topics in Quantum Electronics, Vol. 10, No. 3, 2004, pp. 462–471. <https://doi.org/10.1109/JSTQE.2004.829205>.
- [24] TDK InvenSense, “IAM20380,” , 2024. URL https://invensense.tdk.com/wp-content/uploads/2022/09/DS-000195-IAM-20380_v1.1-Typ.pdf.
- [25] Garbagnati, Elisa and Rüdtenklau, René and Schmidt, Christopher, “Augmenting Attitude Knowledge for Optical Communication Terminals on CubeSats by Kalman Filter Based Estimation,” Proceedings of the Small Satellite Conference, 2025, pp. 1–16. URL <https://digitalcommons.usu.edu/smallsat/2025/RA-S8-2025/4/>.
- [26] Kwon, H. J., Seok, S., and Lim, G., “System modeling of a MEMS vibratory gyroscope and integration to circuit simulation,” Sensors, Vol. 17, No. 11, 2017, p. 2663. <https://doi.org/10.3390/s17112663>.